Torsional properties of helix-reinforced composites fabricated by magnetic freeze casting

Michael M. Porter [a,*], Luis Meraz [b], Albert Calderon [b], Hyunjae Choi [b], Amer Chouhan [b], Leon Wang [c], Marc A. Meyers [a,b,d], Joanna McKittrick [a,b]

[a] Materials Science and Engineering Program, University of California, San Diego, 9500 Gilman Drive, La Jolla, CA 92093, United States
[b] Department of Mechanical and Aerospace Engineering, University of California, San Diego, 9500 Gilman Drive, La Jolla, CA 92093, United States
[c] Department of Bioengineering, University of California, San Diego, 9500 Gilman Drive, La Jolla, CA 92093, United States
[d] Department of Nanoengineering, University of California, San Diego, 9500 Gilman Drive, La Jolla, CA 92093, United States

ARTICLE INFO

ABSTRACT

Helix-reinforced structures are found in a variety of natural materials, from the helical architecture of the narwhal tusk to the Bouligand structures in the exoskeletons of crustaceans. Drawing inspiration from these natural structures, a novel materials processing method, known as magnetic freeze casting, is used to fabricate helix-reinforced hybrid composites. The ZrO_2–epoxy composites investigated here exhibit enhanced torsional properties due their helical architectural organization. In torsion, the maximum tensile and compressive stresses induced by a state of pure shear are oriented at ±45° to the axis of rotation. As a result, the composites with helix-reinforcement oriented parallel to the direction of maximum compressive stress (at ~45°) exhibit the highest shear moduli. Bioinspired, hybrid composites with helix-reinforced structures may be useful for a variety of engineering applications, from the cylindrical shafts in combustion engines to golf clubs and bone implants.

1. Introduction

Helices are found in a variety of natural structures [1], such as the stems of woody plants [2], the skeletons of silica sponges [3], and the tusks of narwhals [4]. These naturally occurring structures grow in response to external stresses and provide reinforcement against induced torsion. Similarly, the double-helix structure of DNA governs its torsional rigidity, an important property that determines its superhelix, tertiary structure [5]. Unlike spirals that have a continuously increasing radius of curvature, such as those commonly found in mollusk shells [6,7] and the horns and antlers of many ruminant mammals [8], helices have a constant radius of curvature and propagate along a central axis [1]. The growth, morphology, and mechanical advantage of spirals and helices observed in natural structures have fascinated scientists for decades [1,9]. Skalak et al. [10] and Harary and Tal [11] developed mathematical models to describe, respectively, the surface growth and morphology of several biological ultrastructures, such seashells, horns, and antlers. At the microstructural level, another form of the helix present in many natural materials is the twisted-plywood or Bouligand structure [12]. This helicoidal structure has been observed in the exoskeletons of crustaceans [13–15] and the scales of fish [16,17]. Recently, it was reported that the twisted nature of the fibrous layers in these materials is mechanically advantageous, enhancing their impact resistance and fracture toughness [15,17].

In modern architectural design, both spirals and helices appear in a variety of synthetic structures, primarily for their natural beauty. However, the helix is also an efficient mechanical design that provides an optimal distribution of stresses in structures subjected to torsional loading (e.g., torsion springs) [18]. Drawing inspiration from this natural design principle, engineering materials that are subjected to external torques may benefit from similar helix-reinforced architectures. Few attempts to utilize the helix for enhanced torsional rigidity in synthetic materials have been reported. Apichattrabrut and Ravi-Chandar [19] and Cheng et al. [20] fabricated helicoidal fiber-reinforced composites that exhibited improved damage tolerance in response to tension, bending, and impact. However, the torsional rigidity of the composites was not investigated [19,20]. Several patents [21–25] on helical reinforced materials have been filed as well. However, to the best of our knowledge, only the torsion transmitting glass shaft

* Corresponding author. Address: Department of Mechanical Engineering, Clemson University, Clemson, SC 29634, United States. Tel.: +1 864 656 1307; fax: +1 864 656 4435.
    E-mail address: mmporte@clemson.edu (M.M. Porter).

invented by Rodgers and Howald [25] utilizes helix-reinforced architectures to improve the torsional rigidity of cylindrical shafts.

Recently, Porter et al. [26] invented a novel materials processing method, known as magnetic freeze casting, to fabricate ceramic scaffolds with helical architectures. This technique expands on conventional freeze casting – a popular method in which a colloidal suspension, typically composed of ceramic particles and water, is directionally frozen, then sublimated to remove the frozen solvent, and sintered to partially densify and strengthen the porous constructs [27,28]. During solidification, the particles are pushed between and trapped within growing ice crystals, leading to lamellar pore channels that are direct replicas of the frozen solvent [27,28]. Subsequently, the porous ceramics can be infiltrated with polymers or metals [29–32], yielding hybrid composites with hierarchical architectures that mimic the natural features of bone (e.g., osteons) or abalone nacre (e.g., brick-and-mortar structures). Although many freeze cast materials exhibit high strength and toughness [29,32], these properties are generally limited to a single direction - parallel to the direction of ice growth.

Magnetic freeze casting uses magnetic fields to manipulate magnetic nanoparticles (i.e., Fe_3O_4) during solidification. This process steers ceramic particles in the direction of the magnetic flux path. Previously, this method was shown to enhance the compressive strength and stiffness of ceramic scaffolds perpendicular to the direction of ice growth, parallel to an applied magnetic field [26]. The enhanced compressive properties obtained are due to the microstructural alignment of lamellar walls in two perpendicular directions: (1) the ice growth direction and (2) the magnetic field direction. In the same study [26], several cylindrical scaffolds with helical architectures were fabricated by rotating magnetic fields about the solidification direction. These scaffolds exhibited biphasic material properties. A circumferential helix composed of a higher-density, Fe_3O_4-rich phase surrounded an interior lower-density, Fe_3O_4-poor phase. The helix was composed of dense lamellar walls aligned parallel to the direction of the prevailing magnetic field. It was proposed that this helical architecture may act as a reinforcing structure, enhancing the torsional rigidity or shear modulus of the material [26,28].

We show herein, both experimentally and analytically, that these helical architectures enhance the torsional rigidity of magnetic freeze cast composites. To do this, it is necessary to compare the shear modulus of composites having identical material compositions, with and without helical architectures. Although several shear test methods currently exist [33,34], the solid-rod torsion test was selected for this work [35]. Previous investigations show that the torsion test is best suited to induce a state of pure shear stress in cylindrical composite samples [35,36]. The method predicts both the shear strength and stiffness of a material from a single test [35,36]. In addition, torsion testing minimizes local material and stress concentration effects as well as unwanted bending moments due to slight misalignments of the samples [35,36]. Experimental measurements of the torsional rigidity (i.e., shear modulus) versus the angle of helix-reinforcement were compared to determine an optimal angle of reinforcement.

2. Materials and methods

2.1. Magnetic freeze casting

Helix-reinforced composite samples were prepared using a custom built freeze cast unit and rotating permanent magnet as previously described [26]. Aqueous slurries of 10 vol.% or 20 vol.% ZrO_2 powders (Sigma Aldrich, St. Louis, MO), with an average diameter of 0.2–0.5 μm, were mixed with 3 wt% (of the total solids) Fe_3O_4 nanoparticles (Sigma Aldrich, St. Louis, MO), with an average

diameter of ∼50 nm, and 1 wt% of each: organic binders, polyethylene glycol (PEG) (Alfa Aesar, Ward Hill, MA) and polyvinyl alcohol (PVA) (Alfa Aesar, Ward Hill, MA), and an ammonium polymethacrylate anionic dispersant, Darvan® 811 (R.T. Vanderbilt Company, Inc., Norwalk, CT). The slurries were ball milled in an alumina grinding medium for 24 h, followed by degassing under low vacuum for 10–20 min. Approximately 3 mL of the degassed slurries were poured into a polyethylene mold with a 9 mm inner diameter and frozen at a constant rate of 10 °C/min. During solidification, a magnetic field of 0.12 T was rotated about the ice growth direction (Z-axis) at 0.05 rpm, 0.20 rpm, or 0.40 rpm, resulting in the helix-reinforced architectures. After freezing, the samples were removed from the mold and lyophilized in a bench-top freeze dryer (Labconco, Kansas City, MO) at −50 °C and 350 Pa for 72 h. The porous green constructs were then sintered in an open air furnace for 3 h at 1300 °C with heating and cooling rates of ±2 °C/min.

Following the sintering process, the porous scaffolds were infiltrated with epoxy (EpoxiCure Resin, Buehler, Lake Bluff, IL), resulting in ceramic–polymer composites with varying volume fractions and angles of helix-reinforcement. To infiltrate the scaffolds, the two-part epoxy solution was first mixed thoroughly for 2–3 min. Then, the porous scaffolds were immersed in the liquid epoxy solution and subjected to a low vacuum for 30 min to degas the solution and infiltrate the scaffolds. After complete infiltration, the wet samples were removed from the liquid epoxy and set at room temperature for 24 h, allowing the epoxy to harden and cure. For clarity, even though the ceramic phase of all the composites contains 3 wt.% Fe_3O_4, it is simply referred to as ZrO_2 throughout this study.

2.2. Material characterization

Scanning electron microscopy (SEM) images were taken at 15 kV on a Philips XL30 field emission environmental scanning electron microscope (FEI-XL30, FEI Company, Hillsboro, OR). For SEM preparation the samples were sputter-coated with iridium using an Emitech K575X sputter coater (Quorum Technologies Ltd., West Sussex, UK).

The thicknesses and angles of helix-reinforcement and the relative volume fractions of the ZrO_2 and epoxy phases of the composites were measured from optical images and scanning electron micrographs using ImageJ software (National Institutes of Health, Bethesda, MD). The helices were measured from optical images using the segment and angle measurements tools. The relative volume fractions were measured from the cross-sections of the composites, where the thresholds of SEM images were adjusted equally to measure the % area of each phase. Four different locations across each cross-section were measured to determine the distribution of densities caused by the rotating magnetic fields.

X-ray diffraction (XRD) was performed on a D2 Phaser X-ray diffraction tool (Bruker AXS, Madison, WI). XRD experiments confirmed that the crystal structure of the ZrO_2 phase remained monoclinic before and after sintering, while a small portion of the Fe_3O_4 phase transformed from magnetite (Fe_3O_4) before sintering to hematite (Fe_2O_3) after sintering at 1300 °C. No apparent transformation due to interactions between the ZrO_2 and Fe_3O_4 phases was observed.

2.3. Torsion testing

The torsional properties of the ZrO_2–epoxy composites with varying volume fractions and different angles of helix-reinforcement were compared using the solid-rod torsion test. The torsion tests were performed on a custom built torsion testing device, capable of twisting the cylindrical composites to induce a state of pure shear stress (see Appendix A).

To test the samples in torsion, the cylindrical ZrO$_2$–epoxy composites were aligned and mounted in epoxy "grips" using a custom built mounting device. All the composite samples were fabricated such that the regions of interest have a circular cross-section of radius r_s ($\sim$7.5 mm) and length L_s ($\sim$25 mm). The epoxy grips of the samples have square cross-sections 25 mm × 25 mm with lengths of L_g ($\sim$25 mm), fitting neatly into the square mounts of the torsion tester. Refer to Appendix A for a complete description of the torsion testing setup and calibration.

Using an empirically derived calibration constant (C = 8.82 × 10^{-4}) and the measured shear modulus of the epoxy grips (G_g = 1.0 GPa), the ultimate shear stress and shear strain at the surface of the ZrO$_2$–epoxy composites were plotted from the experimental data (refer to Appendix A). For simplicity, micromechanics describing the complex nature of the freeze-cast microstructures and the helix-reinforcements were ignored. Instead, the ZrO$_2$–epoxy composites were modeled as orthotropic, elastic materials with unidirectional-reinforcement, similar to that reported by Adams and Thomas [35] and Hamed et al. [37]. Because torsion testing a homogeneous cylinder generates stresses and strains that vary linearly from the central axis of rotation to the outer surface, the maximum shear stress and shear strain occur on the surface of the cylindrical samples. Thus, their ratio, G (shear modulus), is constant, and therefore, provides an accurate description of the torsional rigidity. These assumptions are necessary to compare the effects of ceramic content and helix-reinforcement in the cylindrical composites. Duplicates of each torsion test were run to ensure repeatability.

3. Results and discussion

3.1. Architectural hierarchy

Fig. 1 shows the profiles and cross-sections of eight different ZrO$_2$–epoxy composites fabricated by magnetic freeze casting. As seen in the figure, the two different solid loadings of ZrO$_2$ (10 vol.% and 20 vol.% suspensions) used during the freeze casting process resulted in two sets of composites with varying volume fractions of ZrO$_2$ and epoxy. For clarity, the two sets are referred to as 40:60 and 60:40 composites corresponding to the ZrO$_2$ and epoxy contents, respectively. That is, the 40:60 composites contain $\sim$40 vol.% ZrO$_2$ and $\sim$60 vol.% epoxy, while the 60:40 composites contain $\sim$60 vol.% ZrO$_2$ and $\sim$40 vol.% epoxy (refer to Table 1). The composites have four levels of structural hierarchy: (1) the helix-reinforcement due to the rotating magnetic fields (Fig. 2(a)–(c)); (2) the microstructural alignment due to freeze casting (Fig. 2(d) and (e)); (3) the layered ZrO$_2$–epoxy interface due to polymer infiltration (Fig. 2(f)); (4) the ZrO$_2$ grain structure after sintering and polymer infiltration (Fig. 2(f)).

The distribution of the Fe$_3$O$_4$-rich (brown color) and Fe$_3$O$_4$-poor (white color) phases in the cross-sections of the composites varies considerably (see Fig. 1), while the volume fractions of the two phases on the outer surface were approximately equal (V_A = V_B = 0.5). Fig. 2(a)–(c) show magnified images of the 40:60 composites illustrating the different angles of helix-reinforcement. Increasing the rotation speed of the magnetic field increased the angle, but decreased the thickness of the helices. That is, the 40:60 composites fabricated with a rotating magnetic field at 0.05 rpm had helices $\sim$4 mm thick oriented at an angle of 42°, while those at 0.20 rpm were $\sim$1 mm thick at 73° and those at 0.40 rpm were $\sim$0.5 mm thick at 84°. Similar to that observed by Porter et al. [26], the 40:60 composites showed a distinct separation of the two phases, resulting in biphasic material properties. The Fe$_3$O$_4$ phases in the 60:40 composites, on the other hand, were more homogeneously distributed. However, both sets of composites contain larger volume fractions of ZrO$_2$ in the helical regions. Thus, the helices are more dense and expected to reinforce the structures. Table 1 contains the average volume fractions of ZrO$_2$ in each composite as well as the distribution of ceramic content in the helix-reinforced and non-reinforced regions (respectively labeled as regions A and B, corresponding to Fig. 1). As seen from the data in Table 1, the 40:60 composites contain $\sim$10–15 vol.% more ZrO$_2$ in the helix-reinforced regions (A) than the non-reinforced regions (B), while the 60:40 composites contain only $\sim$5–10 vol.% more ZrO$_2$ in the helix-reinforced regions (A) than non-reinforced regions (B).

Fig. 2(d)–(f) show representative SEM images of the ZrO$_2$ scaffolds after infiltration with epoxy, showing the difference in microstructure and ceramic content in the Fe$_3$O$_4$-poor regions of the 40:60 composites (Fig. 2(d)) and 60:40 composites (Fig. 2(e)). Similarly, the microstructures of the Fe$_3$O$_4$-rich regions resemble those shown in Fig. 2(d) and (e), with slightly higher ceramic contents and some degree of lamellar wall alignment as previously described by Porter et al. [26]. Fig. 2(f) shows that the infiltrated epoxy is well bonded to the ZrO$_2$ scaffolds, completely filling the open porosity. However, the epoxy did not fill any remaining closed porosity existing in the interior of the lamellar walls after sintering the ZrO$_2$ scaffolds. These structural characteristics, namely the helix-reinforcement angle and the relative volume fractions of ZrO$_2$, affect the torsional properties of the composites.

3.2. Torsional properties

Because the ZrO$_2$–epoxy composites are reinforced by a single, continuous helix oriented in a right-handed or clockwise (*CW*) fashion (from the bottom up), the torsional properties of the composites are significantly different depending on the direction of applied torque and the angle of reinforcement. Similarly, the
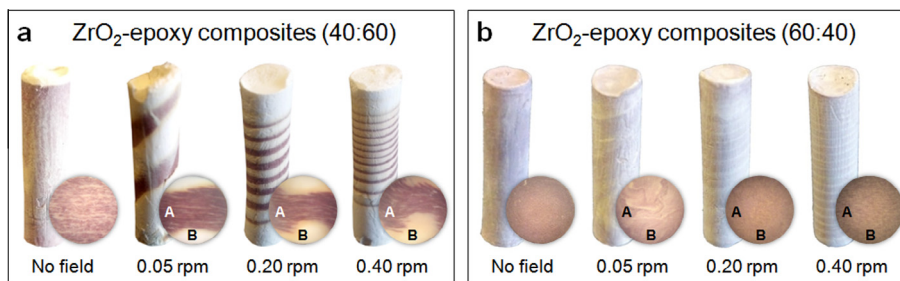

Fig. 1. Representative images of the profiles and cross-sections of the ZrO$_2$–epoxy composites freeze cast under a rotating magnetic field of 0.12 T at the varying rotation speeds shown. (a) ZrO$_2$–epoxy composites composed of $\sim$40 vol.% ZrO$_2$ and $\sim$60 vol.% epoxy. (b) ZrO$_2$–epoxy composites composed of $\sim$60 vol.% ZrO$_2$ and $\sim$40 vol.% epoxy. The letters "A" and "B" shown on the cross-sections represent the Fe$_3$O$_4$-rich helix-reinforced regions and Fe$_3$O$_4$-poor non-reinforced regions, respectively. The diameters of all the composites are $\sim$7.5 mm.

Table 1
Material properties of the aluminum (Al 6061-T6), epoxy, and ZrO_2–epoxy composites, showing the rotation speed of the magnetic field and the resulting helix angle, the average ZrO_2 volume fraction and the ZrO_2 volume fractions of the helix-reinforced (A) and non-reinforced (B) regions corresponding to Fig. 1, the twist direction, and the mechanical shear properties.

Sample type	Rotation speed (rpm)	Helix angle (degrees)	ZrO_2 fraction (vol.%)			Twist direction	Shear strength[b] (MPa)	Shear modulus[b] (GPa)
			Average[a]	A	B			
Al 6061-T6	–	–	–	–	–	CW	207 ± 6	26.0 ± 1.2
Epoxy	–	–	–	–	–	CW	48 ± 2	1.0 ± 0.1
ZrO_2–epoxy composites (40:60)	No field	–	37 ± 4	–	–	CW	36 ± 0	2.5 ± 0.4
	0.05	42	38 ± 10	47	29	CW	37 ± 2	3.1 ± 0.3
	0.20	73	36 ± 5	41	32	CW	46 ± 7	2.8 ± 0.3
	0.40	84	37 ± 6	42	32	CW	48 ± 1	2.6 ± 0.4
ZrO_2–epoxy composites (60:40)	No field	–	58 ± 4	–	–	CW	30 ± 5	2.8 ± 0.8
	0.05	42	59 ± 5	62	55	CW	51 ± 13	5.5 ± 0.7
	0.20	73	57 ± 5	61	54	CW	46 ± 3	4.7 ± 0.7
	0.40	84	59 ± 7	65	53	CW	54 ± 2	4.3 ± 0.5
	0.05	42	63 ± 2	65	61	CCW	35 ± 10	2.8 ± 0.6

[a] Measurements recorded as average ± standard deviation ($n = 4$).
[b] Measurements recorded as average ± standard deviation for Al 6061-T6 ($n = 6$) and epoxy ($n = 6$), and average ± the range of duplicates for ZrO_2–epoxy composites ($n = 2$).

off-axis mechanical behavior of fiber-reinforced laminate composites are dependent on the direction of applied stress and the angle of fiber reinforcement [38]. Therefore, it is convenient to analyze the stress state at the outer surface of the helix-reinforced composites in an analogous fashion to that of a unidirectionally-reinforced plate.

3.2.1. Direction of applied torque

Fig. 3 a compares three 60:40 composites: one with no helix-reinforcement and two with identical helix-reinforcement angles of 42° twisted *CW* and counterclockwise (*CCW*) (see Table 1 for details). The helix-reinforced composite that was twisted in a *CCW* fashion shows little to no improvement over the composite without helix-reinforcement. However, when twisted in the *CW* direction, the 42° helix provides a significant amount of reinforcement, with nearly twice the effective shear modulus (refer to Table 1).

This result is due to the fact that torsion testing induces a state of pure shear stress in the cylindrical samples, as illustrated in Fig. 3(b) and (c). Accordingly, the maximum compressive and

Fig. 2. Architectural hierarchy of the ZrO_2–epoxy composites: (a–c) Representative images of 40:60 composites, illustrating the angle of helix-reinforcement freeze cast under a rotating magnetic field of 0.12 T at varying rotation speeds: (a) 0.05 rpm; (b) 0.20 rpm; (c) 0.40 rpm. (d–f) Representative SEM images of the composites freeze cast under a rotating magnetic field of 0.12 T at 0.20 rpm: (d) 40:60 composites; (e) 60:40 composites; (f) magnified image of the ZrO_2–epoxy interface. The light color is the ZrO_2 phase and the dark color is the epoxy phase. (d,e) The scale bars are 50 µm. (f) The scale bar is 1 µm.

tensile stresses occur on the surface of the cylindrical samples at ±45° (see Fig. 3(b) and (c)). For isotropic materials, the shear modulus (G) is proportional to the elastic modulus (E) and Poisson's ratio (v), according to Eq. (1):

$$G = \frac{E}{2(1 + v)}. \tag{1}$$

Hence, the composite shear modulus can be considered proportional to its elastic modulus ($G \propto E$).

To verify the experimental results observed in Fig. 3(a), the direction of applied torque was analyzed according to the schematics shown in Fig. 3(b)–(e), where a composite with an angle of helix-reinforcement at 45° is twisted: (a) *CW* and (b) *CCW*. Assuming the applied torque induces a state of pure shear and plane stress at the surface of the cylindrical composites, the stress elements shown can be rotated 45° such that the maximum shear stresses (τ_{max}) become maximum compressive and tensile stresses (σ_C and σ_T, respectively), as illustrated in Fig. 3(b)–(e). Now, it becomes convenient to apply the rule-of-mixtures to resolve the compressive and tensile elastic moduli of the composites in directions parallel and perpendicular to the helix-reinforcement [38]. Because the composites are composed of two continuously interpenetrating networks of ZrO_2 and epoxy, the compressive stiffness (E_C) is dominated by the elastic modulus of the ZrO_2 phase, while the tensile stiffness (E_T) is dominated by the ZrO_2–epoxy interfacial adhesion (i.e., interfacial shear or tensile strengths). This suggests that the compressive modulus is much greater than, and dominates, the tensile modulus, such that $E_C \gg E_T$. Therefore, according to the Voigt and Reuss models for unidirectionally-reinforced composite materials [39], and neglecting the tensile moduli, the compressive moduli of the composites can be represented as follows (refer to Fig. 3(d) and (e)):
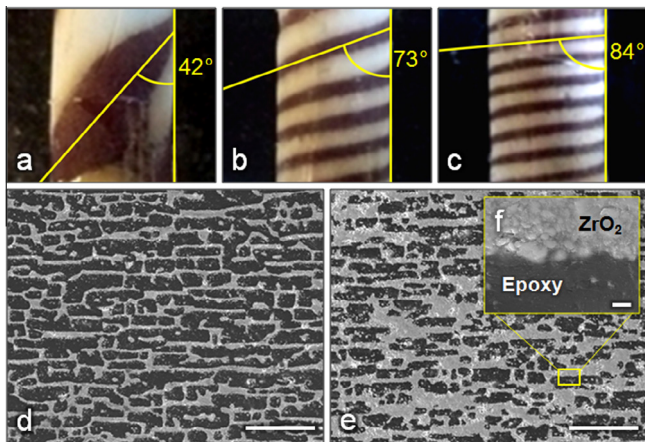
(Fig. 3(d)) The compressive modulus *parallel* to the helix-reinforcement dominates when the applied torque is in the *CW* direction (Voigt model):

$$E_{CW} = V_A E_A + V_B E_B \tag{2}$$

(Fig. 3(e)). The compressive modulus *perpendicular* to the helix-reinforcement dominates when the applied torque is in the *CCW* direction (Reuss model):
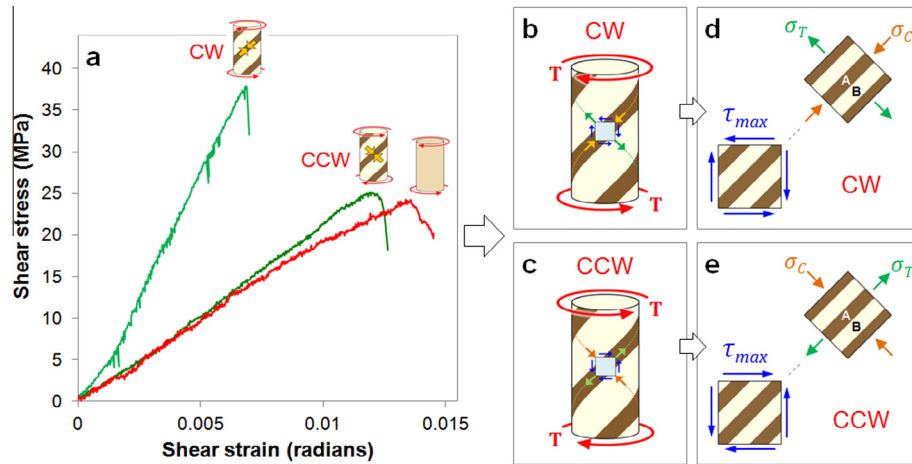
$$\frac{1}{E_{CCW}} = \frac{V_A}{E_A} + \frac{V_B}{E_B}, \tag{3}$$

where E_i is the compressive elastic modulus and V_i is the volume fraction of regions A and B, referring to the helix-reinforced and non-reinforced regions, respectively. As seen in Fig. 3(b)–(e),
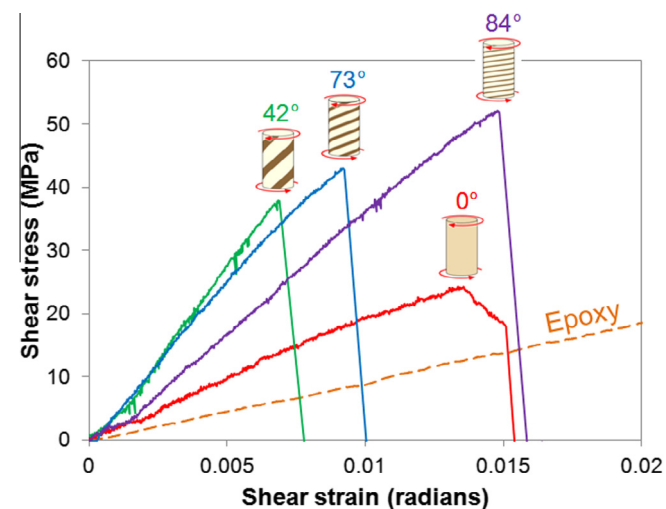
Fig. 3. (a) Surface shear stress–strain curves illustrating the torsional behavior of ZrO₂–epoxy (60:40) composites twisted in different directions. The green curves correspond to 42° helix-reinforced composites and the red curve corresponds to a composite without helix-reinforcement. The helix-reinforced composite was nearly twice as rigid in torsion when twisted in the clockwise (*CW*) direction, as opposed to the counterclockwise (*CCW*) direction. (b–c)Schematics of helix-reinforced composites subjected to a torque (*T*) rotated: (b) *CW* and (c) *CCW*. (d–e) Schematics of a unidirectionally-reinforced plate, illustrative of a stress element at the outer surface of the cylindrical composites, subjected to pure shear and plane stress when twisted: (d) *CW* and (e) *CCW*. The representative stress elements are rotated such that the pure shear stresses (τ_{max}) become pure compressive and tensile stresses (σ_C and σ_T, respectively). The letters "A" and "B" represent the helix-reinforced regions (brown) and non-reinforced regions (white), respectively. (For interpretation of the references to color in this figure legend, the reader is referred to the web version of this article.)

depending on the direction of applied torque, the maximum compressive stresses are oriented (a) parallel or (b) perpendicular to the direction of helix reinforcement. Assuming the increased content of ZrO₂ in the helix-reinforced regions increases the elastic modulus of these regions (E_A), it is concluded that the elastic modulus of the reinforced region is greater than the non-reinforced region ($E_A > E_B$). Thus, the composite must be stiffer when twisted in the *CW* direction, such that $E_{CW} > E_{CCW}$. Based on the assumption from Eq. (1), providing that $G \propto E$, the shear modulus is significantly greater when the applied torque induces a maximum compressive stress parallel to the helix-reinforcement, such that $G_{CW} > G_{CCW}$. In conclusion, the experimental observations presented in Fig. 3(a) agree with the results predicted by this simplified analysis.


Fig. 4. Surface shear stress–strain curves illustrating the torsional behavior of ZrO₂–epoxy (60:40) composites with different angles of helix-reinforcement. The different curves correspond to the different angles of reinforcement, illustrating that the shear modulus (slope) increases as the angle of reinforcement approaches 45°, while the shear strength (maximum stress) increases as the angle of reinforcement approaches 90°. The dashed orange line shows the slope of pure epoxy subjected to torsion. (For interpretation of the references to color in this figure legend, the reader is referred to the web version of this article.)

3.2.2. Angle of helix-reinforcement

In addition to the direction of applied torque, the angle of helix-reinforcement also affects the torsional properties of the composites. To verify this, three composites from each set (40:60 and 60:40) with different angles of helix-reinforcement were twisted in the *CW* direction. Fig. 4 shows the shear stress–strain curves for the 60:40 composites with helix-reinforcement angles of 42°, 73°, and 84°. Comparing the slopes (i.e., shear modulus) of the stress–strain curves, it is obvious that pure epoxy (orange curve in Fig. 4) has the lowest shear modulus (slope) followed by the composite without helix-reinforcement (red curve in Fig. 4), while the 42° composite (green curve in Fig. 4) has the largest shear modulus (refer to Table 1). Fig. 5(a) contains a plot of the measured shear modulus (G_{XY}) versus the angle of helix-reinforcement for both the 40:60 and 60:40 composites. As seen in this plot, it is clear the optimal angle of helix-reinforcement is at 45°. Analogous to the trends predicted by Hamed et al. [37] for filament wound composite tubes, the shear modulus of the 60:40 composites with a reinforcement angle of ~45° (~6 GPa) is roughly twice that of the composites with reinforcement angles of 0° and ~90° (~3 GPa) (refer to Fig. 5(a)). Moreover, increasing the volume fraction of ZrO₂ increased the global shear modulus of the composites, as shown in Fig. 5(a). This is because a larger fraction of ceramic in the helical region on the outer surface of the composites carries a greater amount of the induced maximum shear stresses, since the shear modulus of ZrO₂ is ~90 GPa [40], nearly 100 times greater than that of epoxy (~1 GPa).

Again, assuming a state of pure shear and plane stress at the surface of the cylindrical composites, the results shown in Fig. 5(a) are confirmed by a modified composite laminate theory, following Hyer [38] (refer to Appendix A for complete analysis). Several assumptions were made to simplify the analysis (see Appendix A). Two orthogonal coordinate systems were chosen according to the schematic in Fig. 5(b). The local material coordinates (1, 2, 3) are orthogonal and oriented such that the 1-axis is parallel to the direction of helix-reinforcement. The global material coordinates (X, Y, Z) are orthogonal and oriented such that the *X*-axis is in the circumferential direction, the *Y*-axis is parallel to the cylindrical axis (ice growth direction), and the *Z*-axis, equivalent to the 3-axis, is in the radial direction. The angle of helix-reinforcement (φ) is expressed as the angle, rotated about the
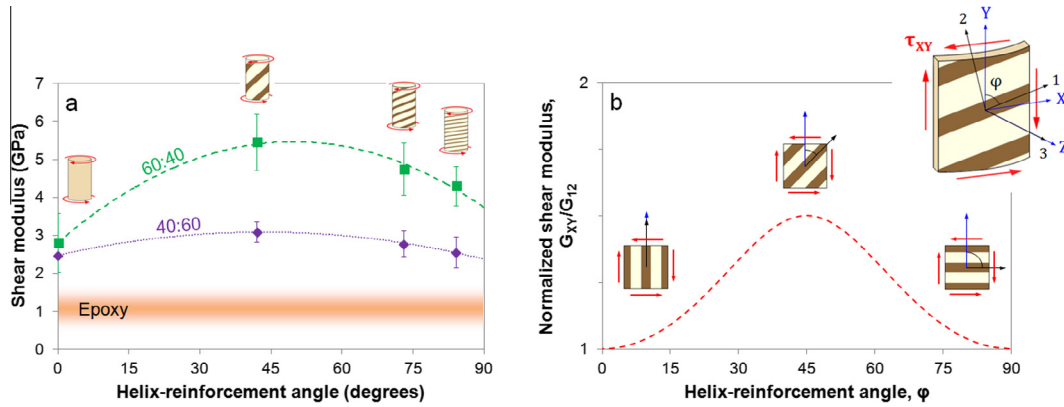
Fig. 5. (a) Plot of the experimental average shear modulus versus the angle of helix-reinforcement for the 60:40 composites (dashed green line) and the 40:60 composites (dotted purple line). The error bars represent the range of data collected for the duplicate samples ($n = 2$). (b) Schematic of the global (X, Y, Z) and local (1,2,3) coordinate systems (upper righthand corner), illustrating the angle of helix-reinforcement (φ) and direction of applied shear stress (τ_{XY}). The plot shows the theoretical normalized shear modulus (G_{XY}/G_{12}, Eqs. (4)–(6)) versus helix-reinforcement angle (φ), assuming the outer surface of the composites as a unidirectionally-reinforced plate subjected to pure shear and plane stress. (For interpretation of the references to color in this figure legend, the reader is referred to the web version of this article.)

Z-axis, between the cylindrical axis (Y-axis) and the reinforcement (1-axis), such that (refer to Fig. 5(b)):

$$m = \cos\left(\frac{\pi}{2} - \varphi\right); \tag{4}$$

$$n = \sin\left(\frac{\pi}{2} - \varphi\right). \tag{5}$$

According to the analysis presented in Appendix A, the normalized shear modulus (G_{XY}/G_{12}) can be expressed in terms of the angle of helix-reinforcement and the material properties in the local coordinate system [38]:

$$G_{XY}/G_{12} = \frac{1}{m^4 + n^4 + 2m^2n^2\left(2\frac{G_{12}}{E_1}(1 + 2v_{12}) + 2\frac{G_{12}}{E_2} - 1\right)}, \tag{6}$$

where G_{XY} is the effective shear modulus of the composite in the XY-plane, G_{12} and v_{12} are the shear modulus and Poisson's ratio in the 12-plane, respectively, and E_1 and E_2 are the elastic moduli of the composite parallel and perpendicular to the helix-reinforcement, respectively, which can be approximated from Eqs. (2) and (3), such that $E_1 \propto E_{CW}$ and $E_2 \propto E_{CCW}$. Fig. 5(b) shows a plot illustrating how the global shear modulus (G_{XY}) on the outer surface of the composites varies with respect to the angle of helix-reinforcement (φ), according to Eqs. (4)–(6). This trend was plotted by ignoring the effect of Poisson's ratio ($v_{12} = 0$) and approximating the elastic properties in the local coordinate system as follows: $E_1 = E_{CW}$, $E_2 = E_{CCW}$, and $G_{12} = E_2/2$ (refer to Eqs. (1)–(3)), where $V_A = V_B = 0.5$ and $E_A = 10 > E_B = 1$. As seen in the plot, the maximum value of the normalized shear modulus (G_{XY}/G_{12}) occurs at an angle of helix-reinforcement of 45°, in agreement with the experimental results (Fig. 5(a)).

Another interesting phenomenon observed in Fig. 4 is that the shear strength of the composites increases as the helix-reinforcement angle increases. This can be explained by the fact that brittle materials subjected to torsion fail in the direction of maximum tension, at 45° to the axis of rotation (refer to Fig. 3(b) and (c)). Most likely, as the angle of the helix-reinforcement approaches 90°, the higher-density, helix-reinforced region deflects or redirects the tensile stresses that occur along the surface of the cylindrical samples. Accordingly, the composites with helix-reinforcement angles at 42° have the lowest shear strength because the helical interface at the Fe_3O_4-rich and Fe_3O_4-poor phases is the weakest point of the structure. When this interface is oriented perpendicular to the maximum tensile stresses, brittle failure occurs at the interface, as explained in the following section.

3.3. Fracture behavior

In torsion, brittle materials typically fail along a 45° angle in the direction of maximum tension (refer to Fig. 3(b) and (c)). Ductile materials, on the other hand, typically fail in the direction of maximum shear, at an angle of 90° to the rotation axis of the applied torque. Fig. 6(a)–(h) show the fracture surfaces of the ZrO_2–epoxy composites. Accordingly, all of the composites fractured at 45° to the rotation axis, perpendicular to the induced maximum tensile stresses (regardless of the twisting direction), suggesting brittle failure. However, upon closer observation of the crack paths (Fig. 6(i)–(l)), it appears that some degree of brittle as well as shear failure occurs in the different composites. Most notably, Fig. 6(j) and (k) show interesting phenomena. In the 42° helix-reinforced composites (Fig. 6(j)), failure occurs at the interface between the helix-reinforced and non-reinforced regions, in the direction of the induced maximum tensile stress. Therefore, the interface separating the two phases (i.e., Fe_3O_4-rich and Fe_3O_4-poor) must be the weakest point of the structure in tension. In the 73° and 84° composites (refer to Fig. 6(k)), the angle of the crack path deviates across each region. This suggests two modes of failure – brittle failure and shear failure – clearly observed in Fig. 6(k), and to a lesser extent in Fig. 6(l). As noted above, the shear strength of the composites increases as the angle of helix-reinforcement increases beyond 45°. Because the maximum tensile stresses induced by torsion are oriented at 45°, characteristic brittle failure seems to occur at the more stiff, but brittle, helix-reinforced (Fe_3O_4-rich) regions, while some instances of shear failure are observed across the non-reinforced regions (see Fig. 6(k)). A possible explanation for this observed crack deflection is that brittle tensile failure in the reinforced regions occurs first and initiates post shear failure in the non-reinforced regions, bridging the crack. This type of crack deflection is commonly observed in a variety of natural materials, such as bone and nacre [41], leading to enhanced strength and toughness.

The modes of failure observed result from mechanisms originating at the microstructural level (Fig. 7). Tensile stresses cause delamination of the epoxy from the ZrO_2 as shown in Fig. 7(a). The debonding of the two phases concentrates local stresses through the ceramic walls, no longer allowing the epoxy to dissipate energy that accumulates between adjacent lamellae. The more prominent mode of failure observed in the composites is brittle fracture. Following delamination, the ceramic walls may be subjected to tensile or compressive stresses (depending on lamellae
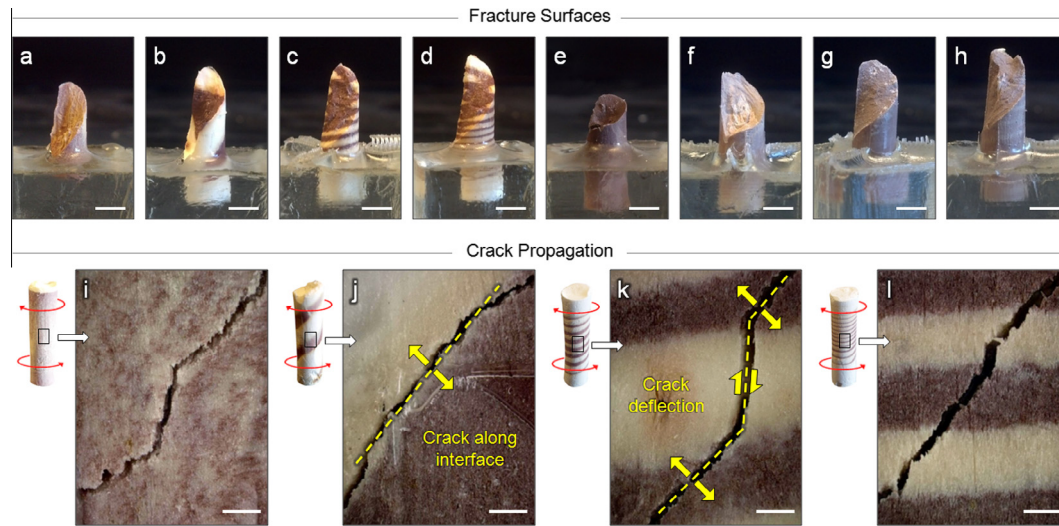
Fig. 6. (Top) Images of the fracture surfaces of ZrO$_2$–epoxy composites loaded in torsion: (a–d) 40:60 composites; (e–h) 60:40 composites; (a, e) no magnetic field; (b, f) 42° helix-reinforcement; (c, g) 73° helix-reinforcement; (d, h) 84° helix-reinforcement. All scale bars are 5 mm. (Bottom) Representative images of the crack path and different failure mechanisms (yellow) due to the torsional loading of ZrO$_2$–epoxy (40:60) composites with different angles of helix-reinforcement: (i) no magnetic field; (j) 42°; (k) 73°; (l) 84°. Images of the cylindrical composites (left) show the direction of applied torque (red arrows) and magnified regions of interest (black boxes). All scale bars are 500 μm. (For interpretation of the references to color in this figure legend, the reader is referred to the web version of this article.)
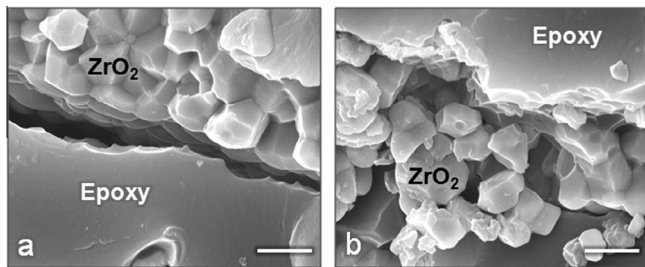
Fig. 7. Fracture surfaces of the ZrO$_2$–epoxy composites, illustrating the two modes of failure: (a) delamination of the epoxy from the ZrO$_2$; (b) crumbling of the ZrO$_2$ lamellar walls due to brittle failure.

orientation and loading direction). In the direction of tensile loading, the lamellae exhibit brittle tensile fracture, while in the direction of compressive loading the lamellae buckle. Fig. 7(b) shows a lamellar wall of ZrO$_2$ that has collapsed and crumbled due to brittle failure. In freeze cast ceramics, it is known that lamellar walls fail by local Euler buckling when subjected to compressive loading [42]. Therefore, after delamination, in the direction of maximum compressive stress, the ZrO$_2$ lamellae may buckle and collapse in a similar manner to that shown in Fig. 7(b). On the other hand, cracks that resemble shear failure (refer to Fig. 6(k)) are caused by interlamellar shearing, which promotes crack propagation through the delaminated ceramic walls as they slide past each other. In conclusion, following delamination due to tensile stresses (Fig. 7(a)), the brittle fracture behavior observed in the helix-reinforced composites (Fig. 7(b)) is governed by two mechanisms occurring in the ceramic phase at the microstructural level: (1) brittle fracture due to tensile or compressive loading of the lamellae and (2) interlamellar shearing of adjacent lamellae.

4. Conclusions

Helix-reinforced ZrO$_2$–epoxy composites fabricated by magnetic freeze casting and subsequent polymer (epoxy) infiltration exhibited exceptional torsional properties. Magnetic fields rotated at different speeds about the ice growth direction were applied to a freeze casting process to steer the magnetic nanoparticles during solidification. The composite materials had hierarchical architectures, with helices composed of higher-density ceramic regions oriented at different angles. Larger volume fractions of the ceramic phase (from ∼40 vol.% to ∼60 vol.%) nearly doubled the shear modulus of the composites. The helix-reinforced structures oriented at ∼45° to the axis of applied torque provided the greatest torsional rigidity when twisted in the clockwise direction, such that the induced maximum compressive stresses propagated parallel to the helix-reinforcement. All of the materials exhibited brittle fracture, primarily governed by three failure mechanisms: delamination of the epoxy from the ZrO$_2$, brittle fracture of ZrO$_2$ lamellae, and interlamellar shearing of adjacent lamellae.

Hybrid composites with hierarchical architectures are promising structural materials for a variety of potential applications [32]. Introducing helix-reinforced structures, as an additional level of hierarchy, may prove beneficial for applications requiring enhanced torsional rigidity. Such applications may include cylindrical shafts used in torque converters for combustion engines and electric motors, sports equipment such as golf clubs or tennis racquets, and axles for wheeled vehicles. Other, less obvious technologies may also benefit from helix-reinforced structures. Freeze cast materials have been proposed as bone implants, having compressive strengths and stiffnesses that nearly match those of natural bone [29,43]. For the practical use of these materials as bone replacements, it becomes necessary to optimize all their mechanical properties, including the torsional rigidity. The method of magnetic freeze casting introduced here is an efficient means to accomplish this goal.

their insightful discussions and assistant with X-ray diffraction experiments. This work is supported by the National Science Foundation, Division of Materials Research, Ceramics Program Grant, 1006931.

Appendix A

A.1. Torsion testing and calibration

The ZrO$_2$–epoxy composites were tested in torsion using a custom built torsion testing device (Fig. A1). The device was attached to the crossheads of a uniaxial Instron materials testing machine (Instron 3367, Norwood, MA) and converts the applied linear displacement of the crosshead to a rotational displacement through a rack and pinion (SR5-500 and SS5-40, Quality Transmission Components, Garden City Park, NY). The rack, attached to the upper crosshead, moves linearly with a tensile (or compressive) load (F) and displacement (d), recorded as a force and displacement by the data acquisition software (Bluehill 2, Instron, Norwood, MA). The linear motion of the rack turns the pinion, converting the applied linear motion to an applied torque (T) and angle of twist (ϕ), such that:

$$T = FR \cos \theta, \tag{A1}$$

$$\phi = \frac{d}{R}, \tag{A2}$$

where R is the pinion radius (100 mm) and θ is the pitch angle of the gear teeth (20°).

To convert the torque-rotation data to shear stress–strain data, an empirical calibration constant ($C = 8.82 \times 10^{-4}$) and the shear modulus of the epoxy grips ($G_g = 1.0$ GPa) were determined. Therefore, to properly calibrate the torsion testing device, a series of six aluminum (Al 6061-T6) samples with a known shear strength (207 MPa), shear modulus (26 GPa), lengths of approximately 40 mm and varying diameters (6 mm, 9 mm, 12 mm) were twisted in the device. The torque-rotation data collected for the aluminum samples of circular cross-section was converted to shear stress–strain data [44,45]:

$$\tau_s = \frac{Tc_s}{J_s}, \tag{A3}$$

$$\gamma_s = \frac{\phi_s c_s}{L_s}, \tag{A4}$$
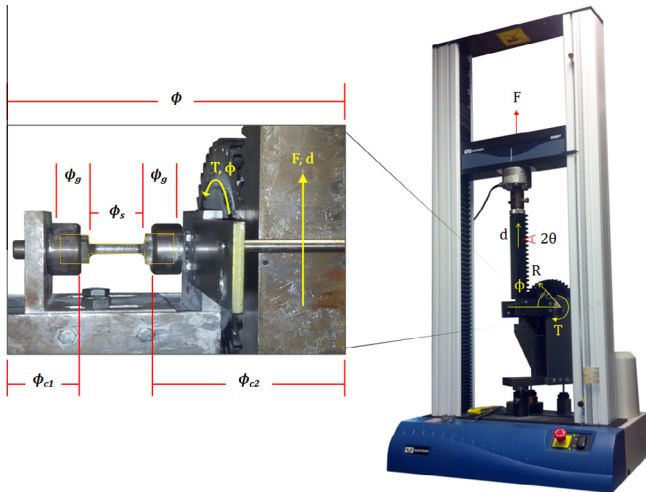
Fig. A1. (a) Torsion testing device, showing the rack and pinion connected to the Instron materials testing machine (right, Instron 3367, Norwood, MA) and a typical torsion sample showing the conversion of force and displacement (F, d) to torque and rotation (T, ϕ).

where τ_s is the surface (or maximum) shear stress, γ_s is the surface (or maximum) shear strain, c_s is the radial distance to the outer most surface of the composite, which in this case is equal to the sample radius ($c_s = r_s$), L_s is the sample length, and J_s is equal to the polar moment of inertia for a shaft of circular cross-section: $J_s = \frac{\pi}{2} r_s^4$. Considering a shaft of square cross-section, however, the maximum shear stress occurs at the point on the surface closest to the center of the shaft, such that Eq. (A3) becomes [44–46]:

$$\tau_s = \frac{4.81T}{b^3}, \tag{A5}$$

where b is the full width of the square cross-section. Similarly, the cross-sections of other noncircular shafts do not remain plane, but warp or bulge, when twisted about their central axis, leading to different geometric effects [44,45]. For a more comprehensive analysis of the shear stress–strain response of noncircular shafts subjected to torsion, refer to [46–49]. Regardless, in this study all samples of interest twisted in the torsion testing device were cylindrical shafts of uniform circular cross-section; thus, Eq. (A5) can be ignored.

Now, assuming that the total angle of twist (ϕ) is the sum of the angles of twist for all of the components subjected to a torque (T) (refer to Fig. A1) [44,45]:

$$\phi = \sum_i \phi_i = \phi_s + 2\phi_g + \phi_{c1} + \phi_{c2}, \tag{A6}$$

the angle of twist of each component can be calculated as [44,45]:

$$\phi_i = \frac{TL_i}{K_i G_i}, \tag{A7}$$

where ϕ_i is angle of twist, L_i is the length, G_i is the shear modulus, and K_i is the warping rigidity factor of component i – referring to the sample of interest (s), the square grips (g), and the device mounts ($c1$ and $c2$), according to Fig. A1. The warping rigidity factor (K_i) depends on the geometry of the cross-section of each component. For the samples of interest, which in this study are all cylindrical shafts of uniform circular cross-section, the warping rigidity factor is equal to the polar moment of inertia [44,45]:

$$K_s = J_s = \frac{\pi}{2} r_s^4. \tag{A8}$$

For the square grips, the warping rigidity factor is [44–46]:

$$K_g = 0.1406 \, b^4, \tag{A9}$$

where the full width of the square grips is b ($\sim$25 mm). Assuming that the geometry and compliance of all the components of the torsion testing device (e.g., mounts) are constant, ϕ_{c1} and ϕ_{c2} can be combined into a single constant value, such that Eq. (A6) can be rewritten as:

$$\phi = T\left(\frac{L_s}{J_s G_s} + 2\frac{L_g}{K_g G_g} + C \right), \tag{A10}$$

where

$$C = \frac{L_{c1}}{K_{c1} G_{c1}} + \frac{L_{c2}}{K_{c2} G_{c2}}. \tag{A11}$$

Next, Eq. (A10) is differentiated with respect to the torque to determine the shear modulus of the sample (G_s) with respect to the slope of the stress–strain curve ($\partial\phi/\partial T$) and the calibration constant (C):

$$\frac{\partial\phi}{\partial T} = \frac{\partial}{\partial T}\left[T\left(\frac{L_s}{J_s G_s} + 2\frac{L_g}{K_g G_g} + C \right) \right]. \tag{A12}$$

Then, setting $G_g = G_s$ because the sample grips and the region of interest of the aluminum samples are composed of the same material, Eq. (A12) can be rewritten as:
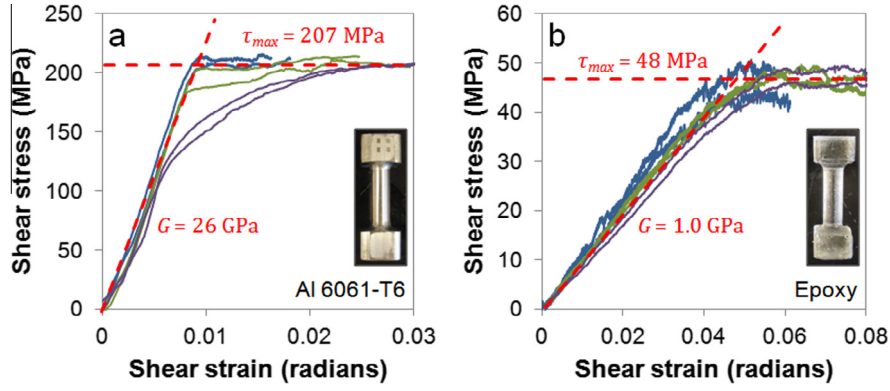
Fig. A2. Shear stress–strain curves: (a) aluminum (Al 6061-T6) samples used to determine the calibration constant ($C = 8.82 \times 10^{-4}$); (b) epoxy samples used to determine the shear modulus of the epoxy grips ($G_g = 1.0$ GPa). The insets show representative images of the dumbbell shaped samples.

$$G_s = \frac{\frac{L_s}{J_s} + 2\frac{L_g}{K_g}}{\frac{\partial \phi}{\partial T} - C}, \tag{A13}$$

where $\partial \phi / \partial T$ is the inverse of the slope of the linear regime of the torque-rotation curve, the values L_s, L_g, J_s, and K_g are all measurable parameters that describe the geometry of the sample, and C is a calibration constant that accounts for the geometry and stiffness of the torsion testing device. Therefore, the ultimate shear stress and shear strain can be plotted using Eqs. (A3) and (A4), where:

$$c_s = r_s, \tag{A14}$$

$$\phi_s = \left[\phi - T\left(2\frac{L_g}{K_g G_g} + C\right)\right]. \tag{A15}$$

Fig. A2(a) shows a plot of the calculated stress–strain curves of the six aluminum samples, using the empirically derived calibration constant:

$$C = 8.82 \times 10^{-4}.$$

As seen in the plot (Fig. A2(a)), the measured shear strength and modulus of aluminum samples are nearly equal to their known values.

Next, to determine the torsional properties of the epoxy used as grips when testing the composites, pure epoxy samples were fabricated and tested. A two part epoxy resin (EpoxiCure Resin, Buehler, Lake Bluff, IL) was degassed under low vacuum and poured into 3D printed molds to form dumbbell shaped samples, like that shown in Fig. A2(b). Six epoxy samples with lengths of approximately 40 mm and varying diameters (6 mm, 9 mm, 12 mm) were tested in torsion. Fig. A2(b) shows the shear stress–strain curves of the epoxy samples, using the above calibration constant. The shear strength and modulus of the epoxy were determined from the plot to be $\sim$48 MPa and $\sim$1.0 GPa, respectively.

Finally, using the empirically derived calibration constant ($C = 8.82 \times 10^{-4}$) and the shear modulus of the epoxy grips ($G_g = 1.0$ GPa), the ultimate surface shear stress and shear strain of the cylindrical ZrO_2–epoxy composites of circular cross-section can be plotted from the experimental data using Eqs. (A3), (A4), (A14) and (A15). Accordingly, the composite maximum shear strength (τ_{max}) and shear modulus (G_s) of the ZrO_2–epoxy composites can be calculated as follows:

$$\tau_{max} = \frac{Tr_s}{J_s}; \tag{A16}$$

$$G_s = \frac{L_s/J_s}{\frac{\partial \phi}{\partial T} - 2\frac{L_g}{K_g G_g} - C}. \tag{A17}$$

A.2. Angle of helix-reinforcement analysis

Referring to Section 3.2.2 and Fig. 5(b), the global elastic moduli (E_X, E_Y) and shear modulus (G_{XY}) of the composites can be predicted analytically, as a function of the angle of helix-reinforcement (φ). Assuming the outer surface of the cylindrical composites is a uni-directionally-reinforced plate subjected to a state of pure shear and plane stress, as illustrated in Fig. 5(b), the stresses on the plate may be reduced as follows:

$$\sigma_X = \sigma_Y = \sigma_Z = \tau_{XZ} = \tau_{YZ} = 0 \tag{A18}$$

and

$$\sigma_3 = \tau_{23} = \tau_{13} = 0. \tag{A19}$$

However, it is important to note that, with the assumption of plane stress, the out-of-plane normal strain is not negligible ($\varepsilon_3 \neq 0$), while the out-of-plane shear strains are reduce to zero ($\gamma_{23} = \gamma_{13} = 0$) [38]. Now, the stresses and strains in the local coordinate system (1, 2, 3) can be expressed in terms of the global coordinate system (X, Y, Z), using the transformation matrix [38]:

$$[T] = \begin{bmatrix} m^2 & n^2 & 2mn \\ n^2 & m^2 & -2mn \\ -mn & mn & m^2 - n^2 \end{bmatrix}, \tag{A20}$$

where $m = \cos\left(\frac{\pi}{2} - \varphi\right)$ and $n = \sin\left(\frac{\pi}{2} - \varphi\right)$, such that:

$$\begin{pmatrix} \sigma_1 \\ \sigma_2 \\ \tau_{12} \end{pmatrix} = [T] \begin{pmatrix} \sigma_X \\ \sigma_Y \\ \tau_{XY} \end{pmatrix} \tag{A21}$$

and

$$\begin{pmatrix} \varepsilon_1 \\ \varepsilon_2 \\ \frac{1}{2}\gamma_{12} \end{pmatrix} = [T] \begin{pmatrix} \varepsilon_X \\ \varepsilon_Y \\ \frac{1}{2}\gamma_{XY} \end{pmatrix}, \tag{A22}$$

where σ_i and τ_{ij} are the normal and shear stresses, and ε_i and γ_{ij} are the normal and shear strains in the (1, 2, 3) and (X, Y, Z) directions, respectively. The relationship between the stresses and strains in the local coordinate system (1, 2, 3) can be expressed by the reduced compliance matrix [S] [38]:

$$\begin{pmatrix} \varepsilon_1 \\ \varepsilon_2 \\ \frac{1}{2}\gamma_{12} \end{pmatrix} = \begin{bmatrix} S_{11} & S_{12} & 0 \\ S_{12} & S_{22} & 0 \\ 0 & 0 & \frac{1}{2}S_{66} \end{bmatrix} \begin{pmatrix} \sigma_1 \\ \sigma_2 \\ \tau_{12} \end{pmatrix}, \tag{A23}$$

where

$$S_{11} = \frac{1}{E_1};$$
$$S_{12} = -\frac{v_{12}}{E_1} = -\frac{v_{21}}{E_2};$$
$$S_{22} = \frac{1}{E_2}; \qquad (A24)$$
$$S_{66} = \frac{1}{G_{12}}$$

and v_{ij} is Poisson's ratio, E_i is the elastic modulus, and G_{ij} is the shear modulus in the $(1,2,3)$ directions, respectively. However, it is necessary to express the global material properties, namely the elastic moduli (E_X, E_Y) and shear modulus (G_{XY}), as functions of the angle of helix-reinforcement (φ) to determine how this angle influences the overall strength and stiffness of the composites subjected to an applied torque. Thus, combining Eqs. (A20)–(A23) yields:

$$\begin{pmatrix} \varepsilon_X \\ \varepsilon_Y \\ \frac{1}{2}\gamma_{XY} \end{pmatrix} = [T]^{-1} \begin{bmatrix} S_{11} & S_{12} & 0 \\ S_{12} & S_{22} & 0 \\ 0 & 0 & \frac{1}{2}S_{66} \end{bmatrix} [T] \begin{pmatrix} \sigma_X \\ \sigma_Y \\ \tau_{XY} \end{pmatrix}, \qquad (A25)$$

which can be rewritten as the transformed reduced compliance matrix $[\overline{S}]$ [38]:

$$\begin{pmatrix} \varepsilon_X \\ \varepsilon_Y \\ \gamma_{XY} \end{pmatrix} = \begin{bmatrix} \overline{S}_{11} & \overline{S}_{12} & \overline{S}_{16} \\ \overline{S}_{12} & \overline{S}_{22} & \overline{S}_{26} \\ \overline{S}_{16} & \overline{S}_{26} & \overline{S}_{66} \end{bmatrix} \begin{pmatrix} \sigma_X \\ \sigma_Y \\ \tau_{XY} \end{pmatrix}, \qquad (A26)$$

where

$$\overline{S}_{11} = S_{11}m^4 + (2S_{12} + S_{66})m^2n^2 + S_{22}n^4;$$
$$\overline{S}_{12} = (S_{11} + S_{22} - S_{66})m^2n^2 + S_{12}(n^4 + m^4);$$
$$\overline{S}_{16} = (2S_{11} - 2S_{12} - S_{66})m^3n - (2S_{22} - 2S_{12} - S_{66})mn^3;$$
$$\overline{S}_{22} = S_{11}n^4 + (2S_{12} + S_{66})m^2n^2 + S_{22}m^4; \qquad (A27)$$
$$\overline{S}_{26} = (2S_{11} - 2S_{12} - S_{66})mn^3 - (2S_{22} - 2S_{12} - S_{66})m^3n;$$
$$\overline{S}_{66} = 2(2S_{11} + 2S_{22} - 4S_{12} - S_{66})m^2n^2 + S_{66}(n^4 + m^4).$$

By analogy (refer to Eqs. (A23) and (A24)), the elastic moduli (E_X, E_Y) and shear modulus (G_{XY}) in the global coordinate system can be expressed in terms of the transformed reduced compliance matrix $[\overline{S}]$ [38]:

$$E_X = \frac{1}{\overline{S}_{11}} = \frac{E_1}{m^4 + m^2n^2\left(\frac{E_1}{G_{12}} - 2v_{12}\right) + n^4\frac{E_1}{E_2}}; \qquad (A28)$$

$$E_Y = \frac{1}{\overline{S}_{22}} = \frac{E_2}{m^4 + m^2n^2\left(\frac{E_2}{G_{12}} - 2v_{21}\right) + n^4\frac{E_2}{E_1}}; \qquad (A29)$$

$$G_{XY} = \frac{1}{\overline{S}_{66}} = \frac{G_{12}}{m^4 + n^4 + 2m^2n^2\left(2\frac{G_{12}}{E_1}(1 + 2v_{12}) + 2\frac{G_{12}}{E_2} - 1\right)}. \qquad (A30)$$

Finally, dividing Eq. (A30) by the local material shear modulus (G_{12}) yields the normalized shear modulus shown in Eq. (6) and plotted in Fig. 5(b):

$$G_{XY}/G_{12} = \frac{1}{m^4 + n^4 + 2m^2n^2\left(2\frac{G_{12}}{E_1}(1 + 2v_{12}) + 2\frac{G_{12}}{E_2} - 1\right)}. \qquad (A31)$$

References

[1] Thompson DAW. On growth and form. Cambridge: Cambridge University Press; 1917.
[2] Skatter S, Kucera B. Spiral grain – an adaptation of trees to withstand stem breakage caused by wind-induced torsion. Holz Als Roh-und Werkst 1997;55(4):207–13.

[3] Weaver JC, Aizenberg J, Fantner GE, Kisailus D, Woesz A, Allen P, et al. Hierarchical assembly of the siliceous skeletal lattice of the hexactinellid sponge Euplectella aspergillum. J Struct Biol 2007;158(1):93–106.
[4] Kingsley MCS, Ramsay MA. The spiral in the tusk of the narwhal. Arctic 1988;41(3):236–8.
[5] Frankkamenetskii MD, Lukashin AV, Anshelevich VV, Vologodskii AV. Torsional and bending rigidity of the double helix from data on small DNA rings. J Biomol Struct Dyn 1985;2(5):1005–12.
[6] Wada K. Spiral growth of nacre. Nature 1966;211(5056):1427.
[7] Yao N, Epstein A, Akey A. Crystal growth via spiral motion in abalone shell nacre. J Mater Res 2006;21(8):1939–46.
[8] Bubenik GA, Bubenik AB. Horns, pronghorns, and antlers: evolution, morphology, physiology, and social significance. New York: Springer; 1990.
[9] Wherry G. Direction of spirals in horns. Nature 1901;63:348.
[10] Skalak R, Farrow DA, Hoger A. Kinematics of surface growth. J Math Biol 1997;35(8):869–907.
[11] Harary G, Tal A. The natural 3D spiral. Comput Graph Forum 2011;30(2):237–46.
[12] Bouligan Y. Twisted fibrous arrangements in biological-materials and cholesteric mesophases. Tissue Cell 1972;4(2):189.
[13] Chen PY, Lin AYM, McKittrick J, Meyers MA. Structure and mechanical properties of crab exoskeletons. Acta Biomater 2008;4(3):587–96.
[14] Raabe D, Sachs C, Romano P. The crustacean exoskeleton as an example of a structurally and mechanically graded biological nanocomposite material. Acta Mater 2005;53(15):4281–92.
[15] Weaver JC, Milliron GW, Miserez A, Evans-Lutterodt K, Herrera S, Gallana I, et al. The stomatopod dactyl club: a formidable damage-tolerant biological hammer. Science 2012;336(6086):1275–80.
[16] Giraud MM, Castanet J, Meunier FJ, Bouligand Y. Fibrous structure of coelacanth scales – twisted plywood. Tissue Cell 1978;10(4):671–86.
[17] Zimmermann EA, Gludovatz B, Schaible E, Dave NKN, Yang W, Meyers MA, et al. Mechanical adaptability of the Bouligand-type structure in natural dermal armour. Nature Commun 2013:4.
[18] Kees Jr G, Worrick III CB, Santangelo JA. Torsion spring. United States: Codman & Shurtleff, Inc.; 1990. US4961743 A.
[19] Apichattrabrut T, Ravi-Chandar K. Helicoidal composites. Mech Adv Mater Struct 2006;13(1):61–76.
[20] Cheng LA, Thomas A, Glancey JL, Karlsson AM. Mechanical behavior of bio-inspired laminated composites. Compos Pt A – Appl Sci Manuf 2011;42(2):211–20.
[21] Antal S, Arvai M, Bartha Z, Gorgenyi P, Meitzen N. Rubber hose with spiral fiber reinforcing core. United States: Taurus Gumiipari Vallalat; 1980. US4241763 A.
[22] Brussee RC. Method of making a filament reinforced pressure vessel. United States: US3282757 A, Structural Fibers; 1966.
[23] Folsom MF. Fiber-reinforced plastic springs with helical fiber wind. United States: US5603490 A, Folsom; Mark F.; 1997.
[24] Mead GNJ. Helical reinforced materials and method of making same. United States: US3449199 A, George NJ Mead; 1969.
[25] Rodgers JJL, Howald AM. Torsion transmitting glass shaft and method of manufacture. United States: Libbey Owens Ford Glass Co; 1951. US2573361 A.
[26] Porter MM, Yeh M, Strawson J, Goehring T, Lujan S, Siripasopsotorn P, et al. Magnetic freeze casting inspired by nature. Mater Sci Eng: A 2012;556(0):741–50.
[27] Deville S. Freeze-casting of porous ceramics: a review of current achievements and issues. Adv Eng Mater 2008;10(3):155–69.
[28] Porter MM, McKittrick J, Meyers MA. Biomimetic materials by freeze casting. JOM 2013:1–8.
[29] Deville S, Saiz E, Nalla RK, Tomsia AP. Freezing as a path to build complex composites. Science 2006;311(5760):515–8.
[30] Launey ME, Munch E, Alsem DH, Barth HB, Saiz E, Tomsia AP, et al. Designing highly toughened hybrid composites through nature-inspired hierarchical complexity. Acta Mater 2009;57(10):2919–32.
[31] Launey ME, Munch E, Alsem DH, Saiz E, Tomsia AP, Ritchie RO. A novel biomimetic approach to the design of high-performance ceramic–metal composites. J R Soc Interface 2010;7(46):741–53.
[32] Munch E, Launey ME, Alsem DH, Saiz E, Tomsia AP, Ritchie RO. Tough, bio-inspired hybrid materials. Science 2008;322(5907):1516–20.
[33] Adams DA. comparison of shear test methods. High-Perform Compos 2005:9–10.
[34] Chiao CC, Moore RL, Chiao TT. Measurement of shear properties of fibre composites: Part 1. Evaluation of test methods. Composites 1977;8(3):161–9.
[35] Adams DF, Thomas RL. The solid-rod torsion test for the determination of unidirectional composite shear properties. Text Res J 1969;39(4):339–45.
[36] Davalos JF, Qiao P, Wang J, Salim HA, Schlussel J. Shear moduli of structural composites from torsion tests. J Compos Mater 2002;36(10):1151–73.
[37] Hamed AF, Megat MH, Sapuan SM, Sahari BB. Theoretical analysis for calculation of the through thickness effective constants for orthotropic thick filament wound tubes. Polym Plast Technol Eng 2008;47(10):1008–15.
[38] Hyer MW. Stress analysis of fiber-reinforced composite materials. Boston: WCB McGraw Hill; 1998.
[39] Park J, Lakes RS. Biomaterials: an introduction. New York: Springer; 2007.
[40] Liu Q-J, Liu Z-T, Feng L-P. Elasticity, electronic structure, chemical bonding and optical properties of monoclinic ZrO2 from first-principles. Phys B: Condens Matter 2011;406(3):345–50.

[41] Ritchie RO. The conflicts between strength and toughness. Nat Mater 2011;10(11):817–22.

[42] Porter MM, Imperio R, Wen M, Meyers MA, McKittrick J. Bioinspired scaffolds with varying pore architectures and mechanical properties. Adv Funct Mater 2013.

[43] Lee S, Porter M, Wasko S, Lau G, Chen P-Y, Novitskaya EE, et al. Potential bone replacement materials prepared by two methods. MRS Online Proc Lib 2012:1418.

[44] Beer FP, Russell E, Johnston J, DeWolf JT. Mechanics of materials. 3rd ed. New York: McGraw-Hill; 2002.

[45] Hibbeler RC. Mechanics of materials. 9th ed. Boston: Prentice Hall; 2013.

[46] Timoshenko S, Goodier J. Theory of elasticity. New York: McGraw-Hill; 1951.

[47] Love AEH. A treatise on the mathematical theory of elasticity. Cambridge University Press; 2013.

[48] Oden JT, Ripperger EA. Mechanics of elastic structures. New York: McGraw-Hill; 1967.

[49] Ugural AC, Fenster SK. Advanced strength and applied elasticity. Pearson Education 2003.